Temperature-dependent changes in the normal albedo of the lunar surface at 1064 nm

Ariel N. Deutsch[1], Gregory A. Neumann[2,] James W. Head[1], Paul G. Lucey[3]

[1]Department of Earth, Environmental and Planetary Sciences, Brown University, Providence RI 02912

[2]NASA Goddard Space Flight Center, Greenbelt, MD 20771

[3]Hawaii Institute of Geophysics and Planetology, University of Hawaii at Manoa, Honolulu, HI, 96822

Corresponding author: Ariel N. Deutsch (ariel_deutsch@brown.edu)

Key Points:

- The Lunar Orbiter Laser Altimeter is sensitive to temperature-dependent changes of normal albedo.
- At 1064 nm, the maria show a slightly stronger negative change in surface reflectance with temperature than the highlands.
- The measured temperature-dependent changes in normal albedo are consistent with the presence of pyroxene at the lunar surface.

Abstract

Over the extreme temperature variations experienced in a single lunar day (ΔT≈300 K), particular minerals common to the lunar surface show spectral changes at near-infrared wavelengths in laboratory settings (Singer and Roush, 1985; Roush and Singer, 1986, 1987). Variations in temperature can cause variations in the size and shape of crystallographic sites, which control the position, shape, and depth of crystal field absorptions. At an observation wavelength of 1064 nm, the Lunar Orbiter Laser Altimeter (LOLA) should be highly sensitive to temperature-dependent changes of orthopyroxene. Here we analyze temperature-dependent spectral changes of the lunar surface as measured from orbit by LOLA. We couple LOLA measurements of normal albedo with measurements of surface temperature from the Diviner Lunar Radiometer Experiment, analyzing the maria and highlands terranes between ±50° in 1°x1° spatial bins. We provide the first evidence of temperature-dependent spectral changes on the lunar surface from orbital observations, finding that the majority of the lunar surface between 50°N and 50°S demonstrates a small, yet measurable, negative change in normal albedo at 1064 nm with temperature ($-\Delta R/\Delta T$). The measurable effect is on the order of a few percent change in reflectance per ~80 K, indicating temperature changes do not have a large effect on measurements of albedo at the sensitivity of the LOLA instrument. Stronger $-\Delta R/\Delta T$ values tend to be associated with the maria, and regions with elevated orthopyroxene levels. Our results suggest that single-wavelength lasers may be powerful tools for understanding the distribution of particular minerals on the lunar surface.

Plain Language Summary

In a single day, the surface temperature of the Moon varies over 300 K (540°F). This massive swing in temperature can affect the ways in which we measure light that is scattered from the lunar surface. The properties of scattered light are important tools for understanding the color and mineralogy of the Moon's surface; therefore, understanding the influence of temperature on these properties is particularly important in interpreting the presence of different rock-forming minerals or ices on the Moon. Here we measure the effect that temperature has on measurements of surface reflectance specifically for the Lunar Orbiter Laser Altimeter, which is an instrument onboard the Lunar Reconnaissance Orbiter and currently orbiting the Moon. We find that there is a small, yet measurable effect where surfaces tend to appear brighter when the surface is colder. This change is consistent with previous laboratory studies of lunar minerals and soils that detected a temperature-dependent change in reflectance properties.

1 Introduction

The thermal environment of the lunar surface is extreme due to the lack of any appreciable atmosphere, the Moon's slow rotation, and the highly insulating nature of the surface (Vasavada et al., 2012). As a result, equatorial surface temperatures drop ~300 K between local noon and night (Williams et al., 2017). Interestingly, over this great temperature range, mafic rock-forming minerals common to the lunar surface (pyroxene and olivine) show spectral changes in the near-infrared (IR) wavelengths (e.g., Singer and Roush, 1985; Roush and Singer, 1986, 1987; Hinrichs and Lucey, 2002). Variations in temperature cause variations in the size and shape of crystallographic sites, which control the position, shape, and depth of crystal field absorptions (Singer and Roush, 1985).

Multiple laboratory studies have demonstrated the near-IR spectral changes that pyroxene and olivine show with respect to temperature (Singer and Roush, 1985; Roush and Singer, 1986, 1987; Hinrichs and Lucey, 2002). For a constant mineralogy, higher temperatures (red colors in Fig. 1) produce a broader absorption band at near-IR wavelengths. In contrast, lower temperatures (blue colors in Fig. 1) result in site contraction, producing a narrower absorption band, an increase in the crystal field splitting energy, and an increase in reflectance (Singer and Roush, 1985; Roush and Singer, 1986, 1987; Hinrichs et al., 1999). The spectral dependence on temperature with wavelength is referred to as the thermo-reflectance spectrum, and can be quantified as the change in reflectance with temperature as a function of wavelength, $\Delta R/\Delta T$, in units of K^{-1} (Hinrichs and Lucey, 2002). Hinrichs and Lucey (2002) demonstrated that the thermo-reflectance spectra of pyroxene and olivine are distinct, and the wavelengths that are most sensitive to the $\Delta R/\Delta T$ of each mineral are unique.

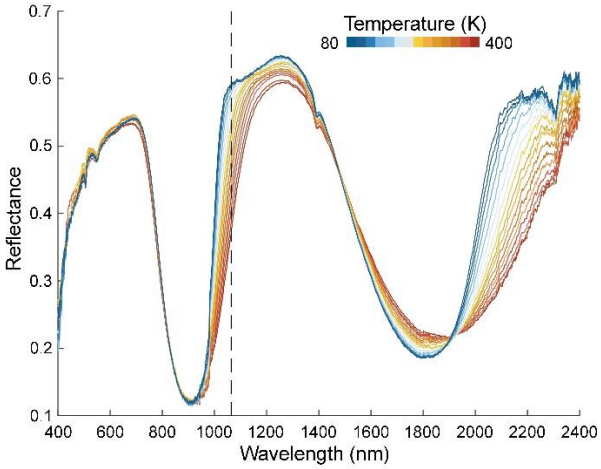

Fig. 1. The reflectances of orthopyroxene (En88) samples that were wet-sieved to 45–90 μm and measured at temperatures between 80 and 400 K by Hinrichs et al. (1999) in the near-IR wavelengths (0.4–2.4 μm). The observation wavelength of LOLA (1064 nm) is marked by the dashed vertical line. At LOLA's wavelength, higher reflectances are measured for orthopyroxenes at lower temperatures than orthopyroxenes at higher temperatures.

The unique thermo-reflectance spectra of pyroxene and olivine have been used previously to characterize the mineralogy of small airless bodies. For example, the spectral properties of Eros as measured by the NEAR-Shoemaker spacecraft were observed to vary with temperature in the near-IR (Lucey et al., 2002). These variations were used to assess the abundance of olivine, and to suggest that Eros has a surface composition similar to that of an LL chondrite (Lucey et al., 2002). Temperature-dependent spectral effects have also been used to explain the differences between the spectra of olivine-rich A-asteroids (observed at low temperatures in space) and the laboratory spectra of olivines (measured in ambient conditions); the spectra of A-asteroids were most similar to laboratory measurements of low-Fe olivines acquired at low temperatures reasonable for the heliocentric distance of the main asteroid belt (Lucey et al., 1998).

Temperature-dependent spectral effects of different rock-forming minerals are dependent on wavelength and one of the largest changes for pyroxene overlaps with the 1064-nm observation wavelength of the Lunar Orbiter Laser Altimeter (LOLA; Smith et al., 2010; 2017)

(Fig. 1). Fig. 2 demonstrates how temperature has a drastic effect on the measured reflectance of pyroxene specifically at LOLA's observing wavelength. Over the range of temperatures experienced by the lunar surface during the course of a single day ($\Delta T \approx 300$ K), low-calcium pyroxene varies in spectral reflectance at 1064 nm by a factor greater than 1.5. Fig. 2 illustrates that at its observation wavelength of 1064 nm, LOLA should be highly sensitive to temperature-dependent changes of orthopyroxene, although not to olivine.

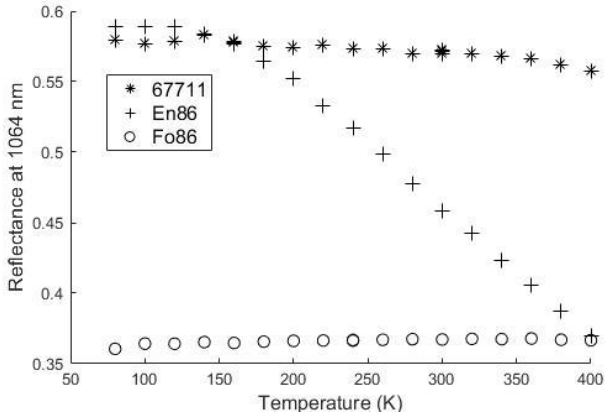

Fig. 2. The thermo-reflectance spectra of lunar minerals and soils at 1064 nm, the observation wavelength of LOLA. The reflectances of orthopyroxene (En88) and olivine (Fo86) were measured by Hinrichs et al. (1999) and the reflectances of Apollo sample 67711 were measured by Hinrichs and Lucey (2002) for a range of temperatures between 80 K and 400 K. LOLA's observation wavelength is strongly sensitive to temperature-dependent spectral changes in orthopyroxene, although not to olivine.

On the lunar surface, which is a complex mixture of many components, there is naturally a more complicated relationship between temperature and reflectance at this wavelength. The abundance of minerals other than pyroxene and also space weathering effects dilute the strong temperature-dependent spectral effects of the pyroxene content. Hinrichs and Lucey (2002) analyzed 11 Apollo soils and found a measureable temperature-dependent spectral effect for the lunar soils (Fig. 2). The change in relative reflectance with temperature was on the order of 1% or less per 100 K, which is substantially less than the 5–10% per 100 K for ordinary chondrites and HEDs or the ~35% per 100 K for pure minerals (Hinrichs and Lucey, 2002). The relative weakness of the $\Delta R/\Delta T$ measured in these specific Apollo samples is likely to be related to (1) the masking effect of submicroscopic iron present in the highly mature soils, (2) the overall low levels of iron in the analyzed samples, and (3) the low sensitivity of the measurements relative to the low-reflectance of the soils analyzed (Hinrichs and Lucey, 2002).

Overall, the few percent variation in reflectance at 1064 nm measured in the Apollo soils over the 100–400 K temperature range is close to the noise level of a single LOLA observation. However, LOLA has been acquiring measurements of the Moon's surface reflectance for nearly a decade (e.g., Smith et al., 2010; Smith et al., 2017), and the tens of millions of LOLA observations enable statistically significant analyses of temperature-dependent changes (Table S1).

Understanding how the reflectance of the lunar surface varies in response to the Moon's drastic thermal environment is important in our interpretations of remotely sensed data, as well as our understanding of the mineralogy of the surface. Specifically, understanding the thermal

response of the lunar surface to solar forcing is important in the characterization of regolith structure and thermophysical properties (e.g., Vasavada et al., 1999, 2012; Hayne et al., 2017; Williams et al., 2017), surface roughness (e.g., Lawrence et al., 2013; Bandfield et al., 2015), and surface rock abundance (Bandfield et al., 2011, 2014; Ghent et al., 2014) and the photometric behavior of the lunar surface (e.g., Barker et al., 2016; Domingue et al., 2018). Furthermore, the optical properties of lunar soils are highly relevant to studies of other airless bodies (e.g., Pieters et al., 2000). Understanding the temperature-dependent spectral behavior of the lunar surface can also help constrain the distribution of specific minerals important in the crustal evolution of the Moon (e.g., Klima et al., 2008, 2011; Lemelin et al., 2019). Furthermore, as additional payloads (with higher resolution and precision) are being prepared to support lunar science and exploration, future remote sensing measurements of the lunar surface should account for temperature changes experienced during observations. This is of particular interest to the volatiles community, given that enhanced reflectance is often used as observational support for the presence of frost and water on airless bodies (e.g., Zuber et al., 2012; Neumann et al., 2013; Deutsch et al., 2017; Ermakov et al., 2017; Fisher et al., 2017).

Thus, here we are interested in how the surface reflectance of the Moon, as measured from orbit by LOLA, changes over the course of a lunar day during its extreme temperature fluctuations. We couple LOLA measurements of lunar surface reflectance with Diviner measurements of lunar surface temperature in order to analyze temperature-dependent changes in highlands and maria reflectance. We discuss implications for using single-wavelength remote sensing instruments as mineralogical sensors, and the importance of accounting for temperature-dependent spectral effects in future exploration of the Moon.

2 Methods and data

2.1 Diurnal changes in the lunar surface reflectance at 1064 nm

LOLA measures the Moon's surface reflectance via the strength of the returned altimetric laser pulse (Smith et al., 2010). Measurements are acquired at a wavelength of 1064 nm, which is coincident with a diagnostic absorption feature of pyroxene (centered near 1 μm) due to the presence of Fe^{2+} in the M2 site of the crystal (Adams, 1974). At LOLA's wavelength, this iron absorption feature has been observed in laboratory studies to reveal strong temperature-dependent spectral changes (Fig. 1) (e.g., Roush and Singer, 1987; Hinrichs et al., 1999).

We analyze the normal albedo of the lunar surface using LOLA data acquired by Detector 3 on Laser 1 during the Nominal Mission Phase (LRO_NO_01 through LRO_NO_13) and the Science Mission Phase (LRO_SM_02 through LRO_SM_17).

Previously, Lemelin et al. (2016) produced calibrated LOLA data that were acquired during the first 10 months of the Nominal Mission Phase. These data were corrected for the sensitivity drift of the lasers with time (i.e., the natural degradation of the lasers) and for anomalous data, which were primarily acquired when the received energy was < 0.14 fJ, when the spacecraft was pointing off-nadir, or when the range was > 70 km (Lemelin et al., 2016). The data were scaled to the normal albedo presented by Lucey et al. (2014), who calibrated LOLA reflectance measurements to Kaguya Multiband Imager observations acquired at zero phase angle at 1050 nm.

In order to increase the spatial and temporal data coverage for this analysis, we supplement Nominal Mission Phase (NO) data with Science Mission Phase (SM) data. Including these additional data more than doubles the coverage in local time (Table S1), allowing for a

more robust statistical analysis. All of the data we use are calibrated to agree with the Lemelin et al. (2016) data, by accounting for the long-term drift of Detector 3 during NO and SM via a cubic polynomial, with a step function offset between the nominal and science mission phases (Fig. S1).

In this calibration, we utilize all daytime data (solar incidence <89°) and discard observations acquired >3° off nadir or during the few days during NO_01 when the laser gains were not fixed (GAINS=FSW). We correct each observation for drift in each mission month and hour of local time (between 07:00 and 16:00) by the polynomial function, and bin the data in 1°x1° spatial bins in order to minimize intrinsic reflectance variations and to suppress thermal blanket anomalies. The data in each local hour for each mission month are regressed between ±25° latitude against the Gridded Data Record Albedo Map LDAM_4 (https://ode.rsl.wustl.edu/mars/pagehelp/quickstartguide/index.html?lola_gdrdam.htm) to obtain the best linear fit to the normal albedo map. The regression coefficients are mapped to the fraction of the LOLA mission month (NO or SM) that they represent, and we fit a cubic polynomial to the slope and a linear polynomial to the intercept to remove the long-term drift in a manner similar to Lemelin et al. (2016), as shown in the Supplemental Material. We use our calibration on both the nominal and science mission phases data to produce our final dataset of lunar normal albedo (Fig. S1).

During the nine years of still ongoing operations, LOLA has nominally collected data throughout the lunar day, although returns are minimal when the LRO spacecraft crosses the terminator due to an artifact introduced from instrument cooling and contraction (Smith et al., 2010); thus, the bulk of calibrated LOLA reflectance data have been acquired between the local hours of 07:00 and 16:00. Our data analysis is limited to local hours of 08:00 and 15:00 to avoid times where the laser blanket anomalies are strongest. Here we analyze the LOLA data for differences in mean normal albedo during the cycle of the lunar day (between the local hours of 08:00 and 15:00) at 1-hr bins by sorting the data based on the local hour at which the data were acquired.

The mean normal albedo at each grid cell (1°x1°) is computed from several thousand individual observations, and our analysis utilizes more than 53 million LOLA observations to enable statistically significant albedo variations (Table S1). We quantify the systematic error by estimating the standard error of the linear comparison of the gridded data with the TC-calibrated data (Lucey et al., 2014) and estimate that the error for our LOLA normal albedo is <3% error. Lemelin et al. (2016) found that the greatest absolute errors in normal albedo (3–4 %) stem from near-nadir geometries and so here we exclude near-nadir observations from our analysis.

Our analysis covers the lunar surface between 50°N and 50°S, latitudes between which temperature fluctuations are greatest (Williams et al., 2017). We find that beyond these latitudes, the blanket thermal anomalies strongly interfere with the laser's measurements of normal albedo. The data are binned in 1°x1° spatial bins, representing surface areas that are ~30x30 km^2. Latitude-dependent reflectance variations associated with space weathering have been observed with LOLA (Lucey et al., 2014; Hemingway et al., 2015; Lemelin et al., 2016; Smith et al., 2017), and thus we limit the extent of each analyzed spatial cell. We also analyze how diurnal changes differ between the highlands and maria, given that these terrains have intrinsically different reflectance properties (e.g., Pieters, 1978; 1986; McEwen et al., 1995; Lucey et al., 2014). We use the lunar maria boundaries as mapped by Nelson et al. (2014) from a 643-nm monochromatic LROC wide-angle camera (WAC) image mosaic, a LROC WAC mosaic

generated from the ratio of band 1 (321 nm) and band 3 (415 nm), and a Clementine color ratio product.

Note that for simplicity, we use the term "reflectance" to mean the normal albedo of the lunar surface, describing the bidirectional reflectance of the surface at zero phase angle; thus, these measurements are independent of illumination conditions.

2.2 Diurnal changes in the lunar surface temperature

The Diviner Lunar Radiometer Experiment characterizes the Moon's thermal environment by mapping the thermal emission from the lunar surface over complete spatial (latitude, longitude) and temporal (diurnal, seasonal) ranges (e.g., Paige et al., 2010; Williams et al., 2017). With the Diviner instrument, we estimate the surface temperature at 1-hr bins between the local hours of 08:00 and 15:00 in order to complement the local time-of-day reflectance measurements from LOLA. We use bolometric temperature data from the Diviner global cumulative product, which provides data at a spatial resolution of 0.5° and a temporal resolution of 0.25 h local time (http://pds-geosciences.wustl.edu/lro/lro-l-dlre-4-rdr-v1/lrodlr_1001/data/gcp/). The bolometric temperature is derived from the brightness temperatures of the individual Diviner spectral channels that measure the Moon's radiance, and is thus a measure of the spectrally integrated flux of IR radiation emerging from the lunar surface (Paige et al., 2010; Williams et al., 2017).

The surface temperature at each grid cell (1°x1°) is calculated from a dataset composed of more than 10 million Diviner observations to enable statistically significant temperature variations. The greatest standard deviations of the Diviner temperature measurements are associated with higher latitude observations, but here our analysis targets only the latitudes between 50°N and 50°S, where associated errors are smallest (Williams et al., 2017). The one-sigma standard deviation of the mean indicates an error of <1.5%.

3 Results

3.1 Temperature-dependent changes in the lunar surface reflectance

Measurements of lunar surface reflectance and temperature for local hours between 08:00 and 15:00 are shown in Fig. 3. During this time window, the surface experiences a maximum temperature change of ~80 K, with peak temperatures around local noon. There is an asymmetry around these peaks due to the thermal inertia of the lunar regolith, such that the surface is slightly warmer in the afternoon (Williams et al., 2017).

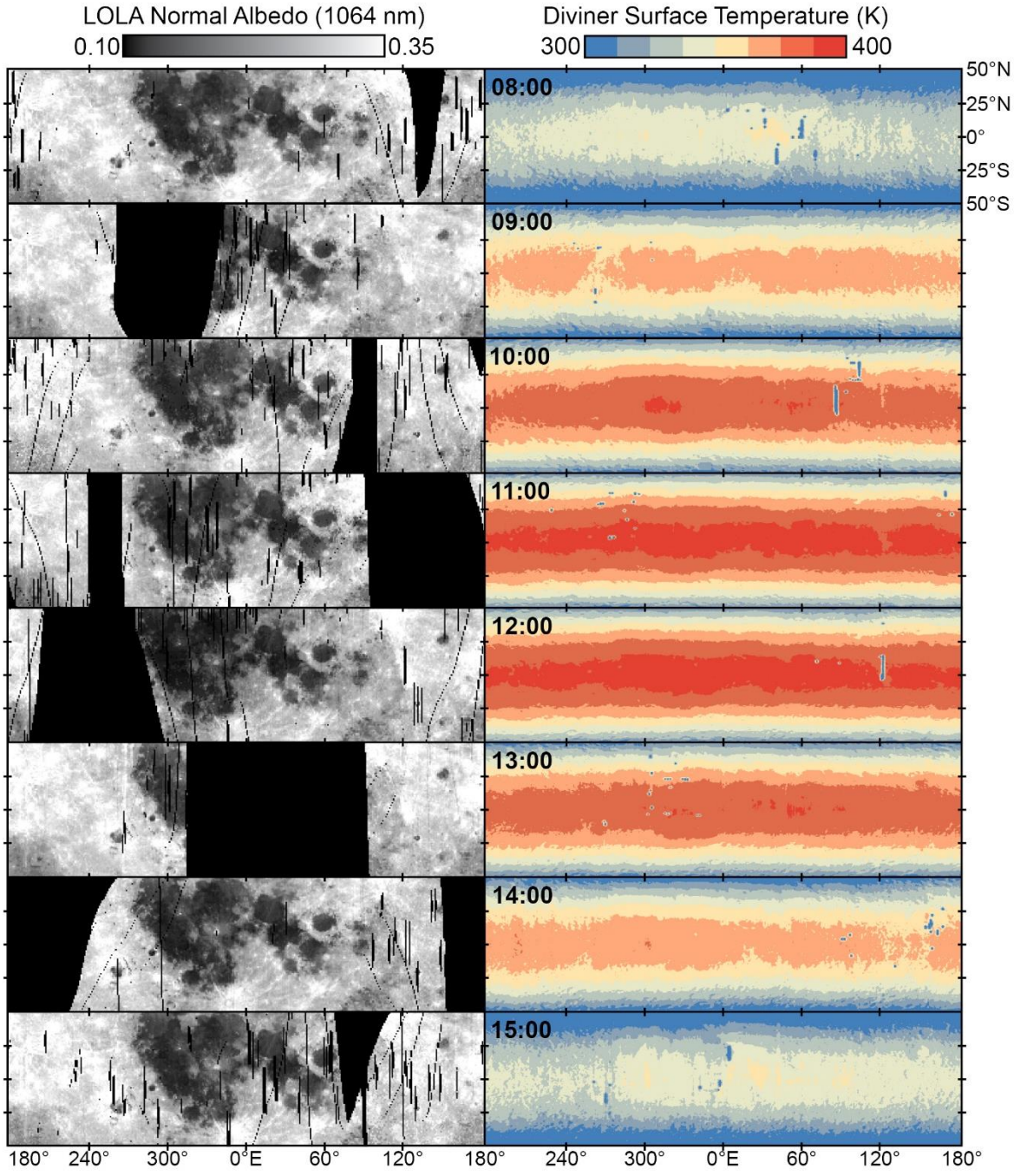

Fig. 3. The LOLA-derived normal albedo at 1064 nm (left) and Diviner-derived temperatures (right) of the lunar surface vary throughout the lunar day. Each row displays the data acquired at a specific hour of local time, between 08:00 and 15:00, and black grids depict regions for which no LOLA data exist. The cylindrically projected maps are centered at 0°E and include latitudes between 50°S and 50°N.

Between the hours of 08:00 and 15:00, there are subtle yet recognizable changes in the measured surface reflectance as measured by LOLA at 1064 nm (Fig. 3). Specifically, the surface appears to have a relatively lower reflectance when it is warmest at 12:00, and appears to have a relatively higher reflectance when the surface is coldest, around 08:00 or 15:00. The most

distinctive changes are easily identifiable in the maria and in the regions immediately adjacent to the maria (Fig. 3).

3.2 The strength of temperature-dependent reflectance changes

In Fig. 4, we quantify the temperature-dependent changes in surface reflectance at 1064 nm. For each degree of latitude between 50°N and 50°S within the highlands and maria, we plot the *mean reflectance* value for each local hour between 07:00 and 15:00 with respect to the *mean surface temperature* value for each local hour between 07:00 and 15:00. For each degree of latitude, we then plot an average thermo-reflectance value ($\Delta R/\Delta T*1000$) by solving for a least-squares fit to the slope (grey lines in Fig. 4). The data are displayed in subplots based on latitude in order to view the $\Delta R/\Delta T$ with clarity. For each of the latitudinal subplots, we solve for the mean thermo-reflectance value ($\Delta R/\Delta T*1000$).

The average thermo-reflectance value ($\Delta R/\Delta T*1000$) reported in each subplot is calculated from the temperature-reflectance relationship of a single degree of latitude, for both the maria and the highlands. As discussed in Section 2, the systematic error of these data is estimated to be <2%. From the associated error of the LOLA and Diviner measurements, we estimate that the uncertainties of our derived thermo-reflectance values to be on the order of 2.5%.

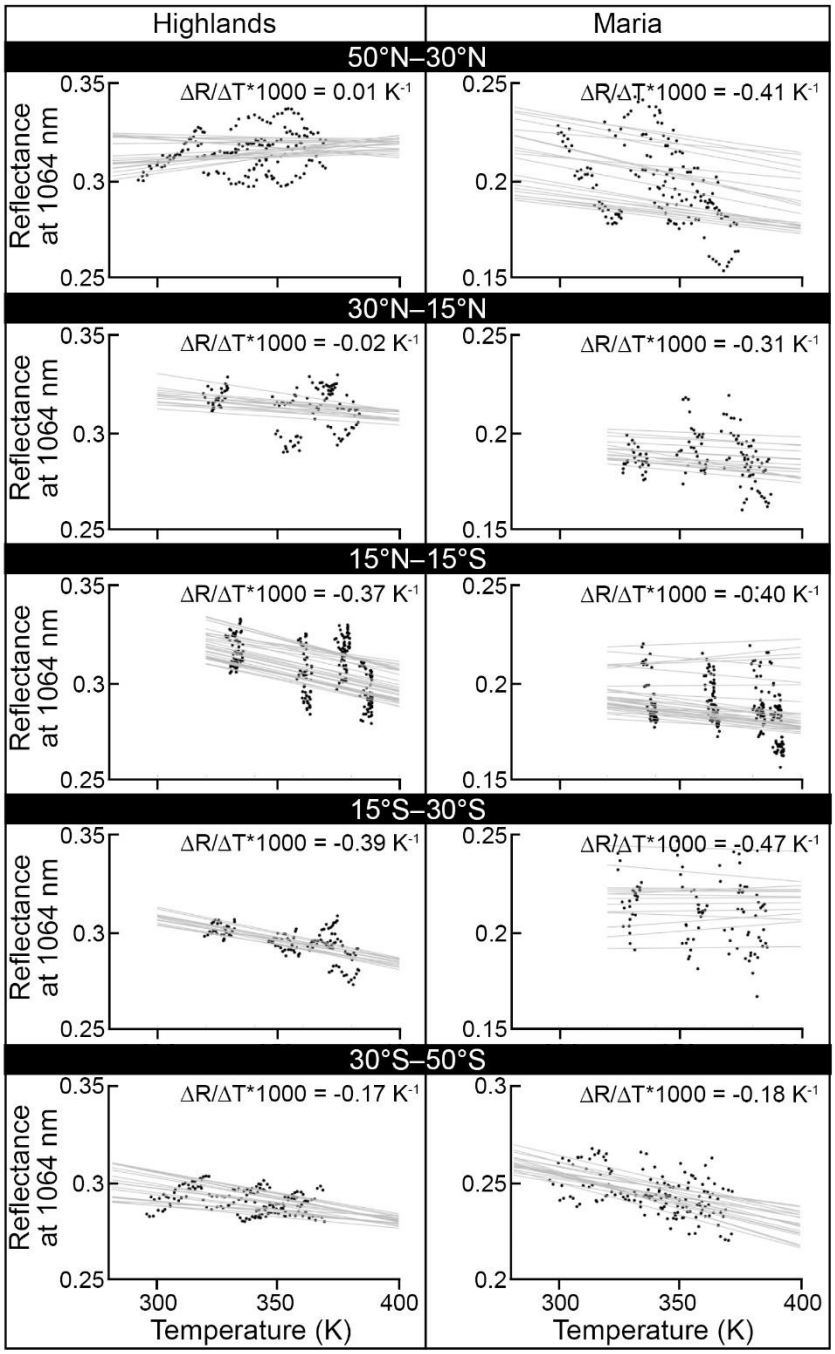

Fig. 4. The 1064-nm surface reflectance of the lunar highlands (left) and maria (right) are shown with respect to the surface temperature during the time of data acquisition. The individual data are plotted as circles and lines of best fit (each derived from a few hundred thousand observations (Table S1)) are shown for each degree of latitude between 50°N and 50°S, representing a single thermo-reflectance value ($\Delta R/\Delta T$). Different latitude ranges are displayed in subplots for clarity. The annual mean surface temperatures for each terrain type for each degree of latitude are correlated by time-of-day to the LOLA data.

We find that the majority of the lunar surface between 50°N and 50°S demonstrates a small, yet measurable, negative change in the surface reflectance at 1064 nm with temperature, consistent with the presence of pyroxene. For 9 of the 10 subplots, the mean $\Delta R/\Delta T$ has a negative slope, indicating a general darkening in the surface reflectance with a warming of the surface. The outlier to this trend is the highlands group between 30°N and 50°N. The maria consistently show stronger $\Delta R/\Delta T$ values than the highlands, meaning that they show a more drastic temperature-dependent change in the measured surface reflectance at 1064 nm. For the maria, the mean $\Delta R/\Delta T*1000$ values are on the order of ~-0.2 to -0.5 K^{-1}. The lunar highlands also tend to show a negative $\Delta R/\Delta T$ trend, although the $\Delta R/\Delta T*1000$ values of the highlands are relatively lower (~0 to -0.4 K^{-1}) than those of the maria. However, for some latitudinal bands, these highland values are nearly equivalent in strength to the $\Delta R/\Delta T$ of the lunar maria (Fig. 4). Pure orthopyroxene has a $\Delta R/\Delta T*1000$ of ~-0.9 K^{-1} at 1064 nm for the temperature range that is experienced by the lunar surface between the local hours of 08:00 and 15:00 (Fig. 2).

Overall, the highlands show the strongest temperature-dependent changes in the equatorial region (15°N – 15°S) and southern mid-latitudes (15°S–30°S). The maria also show the strongest temperature-dependent changes within these regions, although similarly strong changes were detected for the maria between 30°N and 50°N as well. A coarse spatial correlation between the terrane type (Fig. 5b) and the strength of temperature-dependent reflectance changes in reflectance (Fig. 5a) can be observed in Fig. 5.

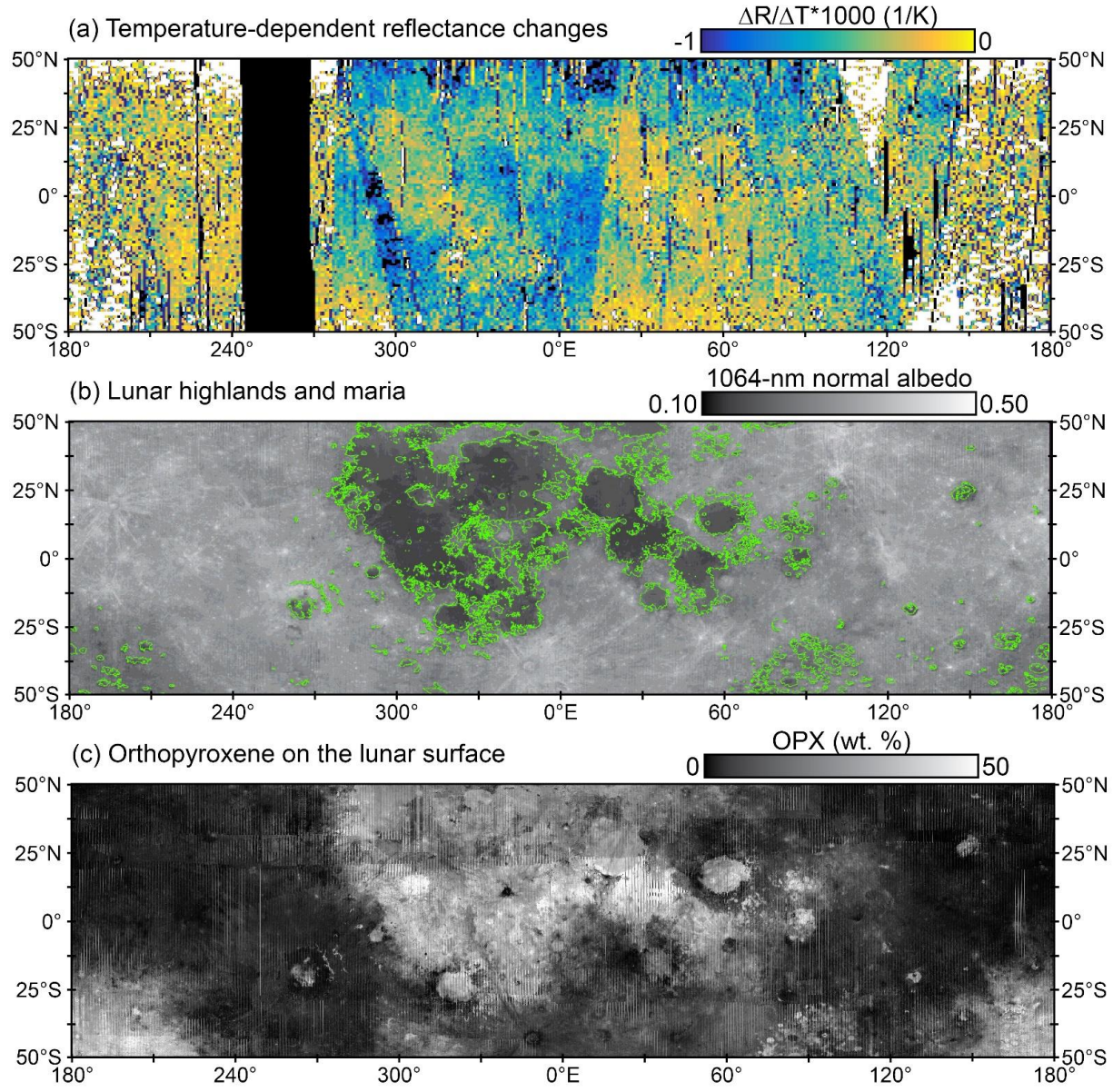

Fig. 5. The temperature-dependent changes in lunar reflectance in panel (a) are compared to the distributions of lunar highlands and maria in panel (b) and of low-calcium pyroxene in panel (c). Specifically, panel (a) expresses the magnitude of temperature-dependent reflectance changes (ΔR/ΔT*1000). All colored pixels (1° x 1° in spatial extent) have higher reflectances at lower temperatures and white pixels either show no change or have lower reflectances at lower temperatures. Black pixels indicate regions with no data. Panel (b) displays the normal albedo of the lunar surface calibrated by Lemelin et al. (2016). Boundaries of the maria are outlined in green, as mapped by Nelson et al. (2014). Panel (c) displays the orthopyroxene abundance on the lunar surface, expressed as weight percent (wt. %), as derived from the Kaguya Lunar MI (Lemelin et al., 2019). All three maps are in a cylindrical projection centered at 0°E and include latitudes between 50°S and 50°N.

This negative relationship between surface reflectance and temperature changes is depicted in Fig. 5(a), where the mean $\Delta R/\Delta T*1000$ values are shown for 1°x1° spatial bins. These values typically range from ~0 to -1 K^{-1}. There are also some anomalous regions on the surface area (shown in white) that experience either a positive or no change in surface reflectance with temperature changes. These regions are typically found along the latitudinal fringes of the study area, where thermal blanket anomalies are most prevalent in the data (Fig. 3).

4 Discussion

4.1 Temperature-dependent spectral changes in the highlands and maria

The results presented here provide the first evidence for temperature-dependent spectral changes of the lunar surface. These results are consistent with laboratory studies that observe a temperature-dependent spectral change for common lunar minerals (Singer and Roush, 1985; Roush and Singer, 1986) and Apollo samples (Hinrichs and Lucey, 2002). Measurements of returned lunar soils revealed a change in relative reflectance with temperature of ~1% or less per 100 K at near-IR wavelengths (Hinrichs and Lucey, 2002). This is similar to the $\Delta R/\Delta T$ that we measure (Fig. 4). We find that this change may be indicative of the mineralogy of the surface (Section 4.2), which suggests important opportunities for understanding surface mineralogy remotely at a single wavelength.

We find that the majority of the lunar surface between 50°N and 50°S demonstrates a small, yet measurable, negative change in the surface reflectance at 1064 nm with temperature; however, our entire study region does not reveal this measurable $\Delta R/\Delta T$ relationship. One factor complicating this analysis is the sensitivity of the LOLA instrument in detecting these extremely small changes in surface reflectance, which are on the order of a few percent change. This change is detected by co-adding the LOLA data that features single shot uncertainty of 12% (Smith et al., 2010), but importantly results from analyzing statistical datasets that include >17 million individual laser shots for each of the local hour groups (Table S1). Thus, we find that our analysis is statistically robust and note that the extremely small changes measured here are comparable to the change in relative reflectance with temperature measured for Apollos soils, which was on the order of 1% or less per 100 K (Hinrichs and Lucey, 2002).

It is also possible that LOLA does not observe a uniformly strong temperature-dependent reflectance change across all the maria or all the highlands due to differences in optical maturity (Hinrichs and Lucey, 2002). Mature soils show less contrast due to the attenuating effect of submicroscopic iron that has accumulated through time from space weathering processes (e.g., Pieters et al., 2000; Hapke, 2001; Pieters and Noble, 2016). The cumulative amount of submicroscopic iron affects the optical properties of measured and modeled soils, resulting in spectral darkening and reddening and subdued absorption bands in the near-IR (e.g., Pieters et al., 2000). Additionally, surfaces that are low in pyroxene will show a weaker temperature-dependent spectral change at LOLA's wavelength (Hinrichs and Lucey, 2002). Changes in absorption band symmetry at 1064 nm occur as Fe^{2+} crystal field absorptions become narrower with decreasing temperature, and these changes are due to the intrinsic absorbance properties of the minerals (Singer and Roush, 1985; Roush and Singer, 1986, 1987; Schade and Wasch, 1999; Moroz et al., 2000; Hinrichs et al., 1999). Finally, the surface reflectance measured by LOLA may also be affected by grain size effects given that varying grain size can cause variations in absolute reflectance at near-IR wavelengths (Adams and Filice, 1967; Pieters, 1983; Clark and Roush, 1984; Pieters et al., 1993; Hapke, 1993, 2012; Mustard and Hays, 1997).

4.2 LOLA as a mineralogical sensor

As discussed in Section 1, different minerals have unique thermo-reflectance spectra that are wavelength-dependent, which have been used in the past to characterize the mineralogy of asteroids (Lucey et al., 1998, 2002). The observation wavelength of LOLA is particularly sensitive to temperature-dependent spectral changes of low-calcium pyroxene (Fig. 2). While it is not commonly considered to be a mineralogical sensor, our results suggest that future laser altimeters as well as LOLA could be used to map the relative abundance of particular minerals (here, pyroxene) from detections of temperature-dependent reflectance changes. Pyroxenes are the most prevalent mafic mineral on the Moon, and are commonly used as a tool for understanding the magmatic source, composition, and cooling history of remotely sensed surfaces (e.g., Adams, 1974; Cloutis and Gaffey, 1991; Sunshine and Pieters, 1993; Greenhagen et al., 2010; Klima et al., 2008, 2011; Yamashita et al., 2012). Understanding the distribution of pyroxene mineralogies is important to our understanding of the crustal evolution on the Moon.

There is substantial heterogeneity in the distribution and abundance of orthopyroxene at the lunar surface (Fig. 5c). Analyses of Kaguya Multiband Imager data indicate that low-calcium pyroxene is abundant (up to ~50 wt.%) in the Procellarum KREEP Terrane and in Mare Tranquilitatis, and is the dominant mafic mineral in the South Pole-Aitken basin (Fig. 5c; Lemelin et al., 2016; 2019). We find that the parts of the surface that do have higher levels of orthopyroxene, indeed show a negative $\Delta R/\Delta T$ relationship (Fig. 5), consistent with laboratory studies (Singer and Roush, 1985; Roush and Singer, 1986; Hinrichs and Lucey, 2002). However, we observe temperature-dependent reflectance changes even on parts of the surface that are orthopyroxene-poor.

In Figure 6, we show the correlation between the amount of orthopyroxene (wt. %) and the thermo-reflectance spectra (K^{-1}) for the highlands (red) and maria (blue). In general, the maria have higher abundances of orthopyroxene exposed at the surface than do the highlands (Lemelin et al., 2019). We find that, on average, the maria also have stronger negative $\Delta R/\Delta T$ values, as indicated by the spread of data shifted to the left in the box plot below Fig. 6. This trend suggests that the mare surfaces show a slightly larger change in the surface reflectance at 1064 nm between the local hours or 08:00 and 15:00 than do the highlands.

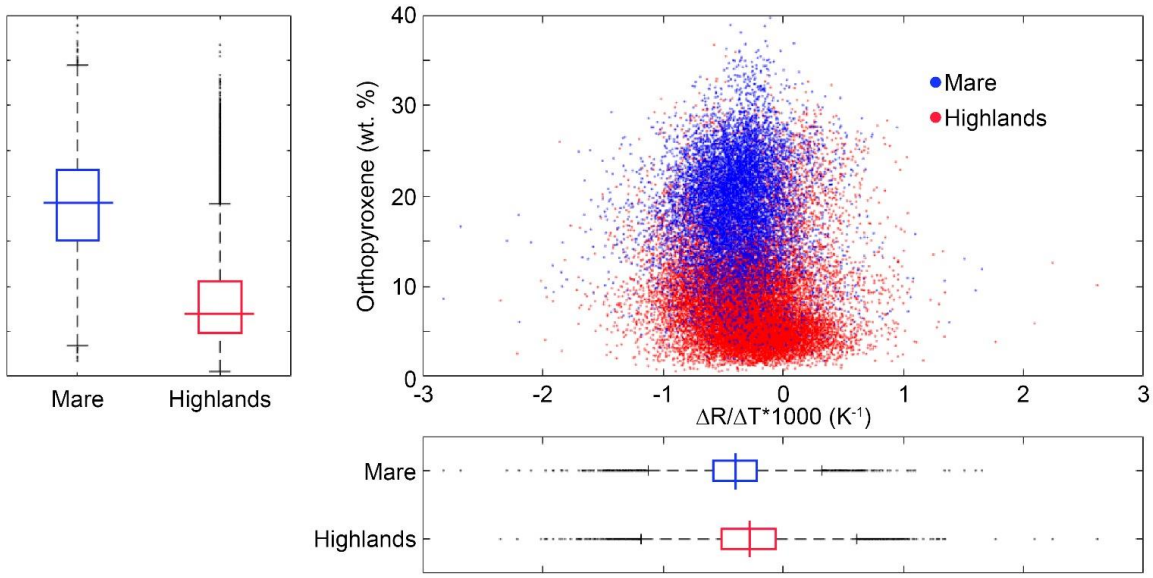

Fig. 6. The correlation between temperature-dependent reflectance changes (ΔR/ΔT*1000) and orthopyroxene abundance (wt. %) within the lunar highlands (red) and maria (blue).

We also note that there is considerable overlap between the ΔR/ΔT values calculated for the maria and highlands. Thus, there are likely to be other factors that are influencing how different regions of the surface experience the changes of surface reflectance as measured by LOLA during these different times of day. Figure 5 shows that the greatest temperature-dependent changes in reflectance are concentrated near the boundaries of the maria. There are likely to be some mixing effects between the boundaries of the maria and highlands, given that these contacts are diffuse due to mixing processes through time (Fischer and Pieters, 1995; Li and Mustard, 2000; 2003; 2005). Spectral mixture analyses indicate that large impact craters have resulted in highland contamination of the spectral properties of mare surfaces (Li and Mustard, 2002), as lateral transport is more efficient than vertical transport during mixing along these boundaries (Li and Mustard, 2000).

As discussed in Section 4.1., other factors that complicate thermo-reflectance spectra may include differences in iron levels, grain size, or optical maturity. For example, the absorption features of mature surfaces are relatively subdued as a result of space weathering processes (e.g., Pieters et al., 1993; 2000; Lucey et al., 2000; Noble et al., 2001). The optical maturity index derived by Lucey et al., 2000 indicates that lunar surface maturity is partly dependent on geologic setting, given that crater interiors tend to mature more slowly compared to their ejecta and that larger ejecta features tend to mature more slowly than smaller features. Generally, Copernican surfaces are relatively more immature compared to older surfaces, and the index appears to saturate near the age of Copernicus (Lucey et al., 2000). The most immature surface on the lunar surface today include surfaces near Tycho, Stevinus, Giordano Bruno, and some northern highlands, between De La Rue, Hayn, and Bel'kovich craters. These regions tend to show stronger ΔR/ΔT values (Fig. 5), consistent with the understanding that more immature surfaces exhibit stronger contrast in absorption features.

We also observe heterogeneity in the strength of ΔR/ΔT values within the mare deposits (Fig. 5a), which vary in orthopyroxene abundances (Fig. 5c; Lemelin et al., 2016; 2019) as well as in age (e.g., Hiesinger et al. 2003; 2010; 2011). The mineralogy of mare basalts shows both

temporal and spatial heterogeneity. For example, young Oceanus Procellarum basalts are rich in olivine and show a stratigraphic gradation with underlying units of lower olivine abundance, while young Orientale basalts are olivine-poor and rich in high-Ca pyroxene (Varatharajan et al., 2014). This heterogeneity suggests variability in FeO content in younger basalts across the Moon (Varatharajan et al., 2014), and such heterogeneity may affect the strength of the temperature-dependent signal detected here.

5 Conclusions

We have documented the first evidence of temperature-dependent spectral changes on the lunar surface from orbital observations. Our statistical analysis, incorporating more than 53 million individual LOLA shots, indicate that temperature variations do have a measurable effect on the reflectance of the surface at 1064 nm wavelength. Specifically, measurements of higher reflectance were acquired by LOLA when the surface temperatures of the Moon were lower. The measurable effect discussed here is on the order of a few percent change in reflectance per ~80 K, indicating that temperature changes do not have a large effect on measurements of the lunar surface at the sensitivity of the LOLA instrument.

An ability to understand how the lunar surface varies with temperature will provide important constraints for future remote sensing observations of the Moon. Such observations can help assess the relative abundance of particular rock-forming minerals (here, pyroxene) that exhibit a change in spectral reflectance with temperature, completely independent of spectroscopic methods.

Temperature-dependent spectral changes have important implications for future remotely sensed observations of the Moon, as additional lasers and spectrometers with higher resolution and precisions are designed and operated. These results suggest that additional laser wavelengths targeted at olivine can provide independent data for the distribution of that mineral. Of particular interest is understanding these effects on interpretations of the presence of surface volatiles. Both the science and exploration communities have strong interests in the presence of surface ice on the Moon (and beyond). Enhanced surface reflectance has been used to characterize the presence of surface ice not only on the Moon (e.g., Zuber et al., 2012; Fisher et al., 2017; Qiao et al., 2018), but also on Mercury (Neumann et al., 2013; Chabot et al., 2014; Deutsch et al., 2017), smaller airless bodies (e.g., Platz et al., 2016; Ermakov et al., 2017), Mars (e.g., Smith et al., 1998; Bell et al., 1999), and beyond. Thus, understanding how temperature affects observations of surface reflectance has widespread importance in the planetary community.

Acknowledgements

This work is supported by NASA issued through the Harriett G. Jenkins Graduate Fellowship to A.N.D. (Grant Number NNX16AT19H), by the NASA Discovery Program to G.A.N, by NASA-Goddard to J.W.H. for participation in the Lunar Reconnaissance Orbiter (LRO) Lunar Orbiter Laser Altimeter (LOLA) Experiment Team (NNX11AK29G, NNX13AO77G and 80NSSC19K0605), and also by the LRO LOLA Experiment to P.G.L.

Data availability statement

The uncalibrated LOLA normal albedo data used in this study can be accessed from the LOLA PDS Data Node at http://imbrium.mit.edu/DATA/LOLA_RADR/laser1/. The Diviner temperature data can be accessed at http://pds-geosciences.wustl.edu/lro/lro-l-dlre-4-rdr-

v1/lrodlr_1001/data/gcp/. The Kaguya Lunar Multiband Imager data of surface orthopyroxene content can be accessed at https://astrogeology.usgs.gov/search/map/Moon/Kaguya/MI/MineralMaps/Lunar_Kaguya_MIMap_MineralDeconv_OrthopyroxenePercent_50N50S.

References

Adams, J. B. (1974). Visible and near-infrared diffuse reflectance spectra of pyroxenes as applied to remote sensing of solid objects in the solar system. *Journal of Geophysical Research*, *79*(32), 4829–4836. https://doi.org/10.1029/JB079i032p04829.

Adams, J. B., & Filice, A. L. (1967). Spectral reflectance 0.4 to 2.0 microns of silicate rock powders. *Journal of Geophysical Research (1896-1977)*, *72*(22), 5705–5715. https://doi.org/10.1029/JZ072i022p05705.

Bandfield, J. L., Ghent, R. R., Vasavada, A. R., Paige, D. A., Lawrence, S. J., & Robinson, M. S. (2011). Lunar surface rock abundance and regolith fines temperatures derived from LRO Diviner Radiometer data. *Journal of Geophysical Research: Planets*, *116*(E12). https://doi.org/10.1029/2011JE003866.

Bandfield, J. L., Hayne, P. O., Williams, J.-P., Greenhagen, B. T., & Paige, D. A. (2015). Lunar surface roughness derived from LRO Diviner Radiometer observations. *Icarus*, *248*, 357–372. https://doi.org/10.1016/j.icarus.2014.11.009.

Bandfield, J. L., Song, E., Hayne, P. O., Brand, B. D., Ghent, R. R., Vasavada, A. R., & Paige, D. A. (2014). Lunar cold spots: Granular flow features and extensive insulating materials surrounding young craters. *Icarus*, *231*, 221–231. https://doi.org/10.1016/j.icarus.2013.12.017.

Barker, M.K., Sun, X., Mazarico, E., Neumann, G.A., Zuber, M.T., & Smith, D.E. (2016). Lunar phase function at 1064 nm from Lunar Orbiter Laser Altimeter passive and active radiometry. *Icarus, 273*, 96–113. https://doi.org/10.1016/j.icarus.2016.02.008.

Bell, J. F., Wolff, M. J., Daley, T. C., Crisp, D., James, P. B., Lee, S. W., et al. (1999). Near-Infrared Imaging of Mars from HST: Surface Reflectance, Photometric Properties, and Implications for MOLA Data. *Icarus*, *138*, 25–35. https://doi.org/10.1006/icar.1998.6057.

Chabot, N. L., Ernst, C. M., Denevi, B. W., Nair, H., Deutsch, A. N., Blewett, D. T., et al. (2014). Images of surface volatiles in Mercury's polar craters acquired by the MESSENGER spacecraft. *Geology*, *42*, 1051–1054. https://doi.org/10.1130/G35916.1.

Clark, R. N., & Roush, T. L. (1984). Reflectance spectroscopy: Quantitative analysis techniques for remote sensing applications. *Journal of Geophysical Research: Solid Earth*, *89*(B7), 6329–6340. https://doi.org/10.1029/JB089iB07p06329.

Cloutis, E. A., & Gaffey, M. J. (1991). Pyroxene spectroscopy revisited: Spectral-compositional correlations and relationship to geothermometry. *Journal of Geophysical Research: Planets*, *96*(E5), 22809–22826. https://doi.org/10.1029/91JE02512.

Deutsch, A. N., Neumann, G. A., & Head, J. W. (2017). New evidence for surface water ice in small-scale cold traps and in three large craters at the north polar region of Mercury from the Mercury Laser Altimeter. *Geophysical Research Letters*, *44*, 9233–9241. https://doi.org/10.1002/2017GL074723.

Domingue, D., Palmer, E., Gaskell, R., & Staid, M. (2018). Characterization of lunar surface within Tsiolkovsky crater: Photometric properties. *Icarus*, *312*, 61–99. https://doi.org/10.1016/j.icarus.2018.02.034.

Ermakov, A. I., Mazarico, E., Schröder, S. E., Carsenty, U., Schorghofer, N., Preusker, F., et al. (2017). Ceres's obliquity history and its implications for the permanently shadowed regions. *Geophysical Research Letters*, *44*(6), 2652–2661. https://doi.org/10.1002/2016GL072250.

Fischer, E. M., & Pieters, C. M. (1995). Lunar surface aluminum and iron concentration from Galileo solid state imaging data, and the mixing of mare and highland materials. *Journal of Geophysical Research: Planets*, *100*(E11), 23279–23290. https://doi.org/10.1029/95JE02359.

Fisher, E. A., Lucey, P. G., Lemelin, M., Greenhagen, B. T., Siegler, M. A., Mazarico, E., et al. (2017). Evidence for surface water ice in the lunar polar regions using reflectance measurements from the Lunar Orbiter Laser Altimeter and temperature measurements from the Diviner Lunar Radiometer Experiment. *Icarus*, *292*, 74–85. https://doi.org/10.1016/j.icarus.2017.03.023.

Ghent, R. R., Hayne, P. O., Bandfield, J. L., Campbell, B. A., Allen, C. C., Carter, L. M., & Paige, D. A. (2014). Constraints on the recent rate of lunar ejecta breakdown and implications for crater ages. *Geology*, *42*(12), 1059–1062. https://doi.org/10.1130/G35926.1.

Greenhagen, B. T., Lucey, P. G., Wyatt, M. B., Glotch, T. D., Allen, C. C., Arnold, J. A., et al. (2010). Global Silicate Mineralogy of the Moon from the Diviner Lunar Radiometer. *Science*, *329*(5998), 1507–1509. https://doi.org/10.1126/science.1192196.

Hapke, B. (1993). Theory of Reflectance and Emittance Spectroscopy by Bruce Hapke. https://doi.org/10.1017/CBO9780511524998.

Hapke, B. (2001). Space weathering from Mercury to the asteroid belt. *Journal of Geophysical Research: Planets*, *106*(E5), 10039–10073. https://doi.org/10.1029/2000JE001338.

Hapke, B. (2012). Theory of Reflectance and Emittance Spectroscopy by Bruce Hapke. https://doi.org/10.1017/CBO9781139025683.

Hayne, P. O., Bandfield, J. L., Siegler, M. A., Vasavada, A. R., Ghent, R. R., Williams, J.-P., et al. (2017). Global regolith thermophysical properties of the Moon from the Diviner Lunar Radiometer Experiment. *Journal of Geophysical Research: Planets*, *122*(12), 2017JE005387. https://doi.org/10.1002/2017JE005387.

Hiesinger H., Head J. W., Wolf U., Jaumann R., & Neukum G. (2003). Ages and stratigraphy of mare basalts in Oceanus Procellarum, Mare Nubium, Mare Cognitum, and Mare Insularum. *Journal of Geophysical Research: Planets*, *108*(E7), 5065. https://doi.org/10.1029/2002JE001985.

Hiesinger, H., Head, J.W., Wolf, U., Jaumann, R., & Neukum, G. (2011). Ages and stratigraphy of lunar mare basalts: A synthesis. *Geological Society of America Special Papers*, *477*, 1–51. https://doi.org/10.1130/2011.2477(01).

Hiesinger, H., Head, J.W., Wolf, U., Jaumann, R., Neukum, G., 2010. Ages and stratigraphy of lunar mare basalts in Mare Frigoris and other nearside maria based on crater size-frequency distribution measurements. *Journal of Geophysical Research: Planets*, *115*, E03003. https://doi.org/10.1029/2009JE003380.

Hinrichs, J. L., & Lucey, P. G. (2002). Temperature-dependent near-infrared spectral properties of minerals, meteorites, and lunar soil. *Icarus*, *155*(1), 169–180. https://doi.org/10.1006/icar.2001.6754.

Hinrichs, J. L., Lucey, P. G., Robinson, M. S., Meibom, A., & Krot, A. N. (1999). Implications of temperature-dependent near-IR spectral properties of common minerals and meteorites

for remote sensing of asteroids. *Geophysical Research Letters*, *26*(12), 1661–1664. https://doi.org/10.1029/1999GL900334.

Klima, R. L., Pieters, C. M., & Dyar, M. D. (2008). Characterization of the 1.2 μm M1 pyroxene band: Extracting cooling history from near-IR spectra of pyroxenes and pyroxene-dominated rocks. *Meteoritics & Planetary Science*, *43*(10), 1591–1604. https://doi.org/10.1111/j.1945-5100.2008.tb00631.x.

Klima, R. L., Pieters, C. M., Boardman, J. W., Green, R. O., Head, J. W., Isaacson, P. J., et al. (2011). New insights into lunar petrology: Distribution and composition of prominent low-Ca pyroxene exposures as observed by the Moon Mineralogy Mapper (M3). *Journal of Geophysical Research: Planets*, *116*(E6). https://doi.org/10.1029/2010JE003719.

Lawrence, S. J., Stopar, J. D., Hawke, B. R., Greenhagen, B. T., Cahill, J. T. S., Bandfield, J. L., et al. (2013). LRO observations of morphology and surface roughness of volcanic cones and lobate lava flows in the Marius Hills. *Journal of Geophysical Research: Planets*, *118*(4), 615–634. https://doi.org/10.1002/jgre.20060.

Lemelin, M., Lucey, P. G., Gaddis, L. R., Hare, T., & Ohtake, M. (2016). Global map products from the Kaguya Multiband Imager at 512 ppd: Minerals, FeO and OMAT. 47th LPSC, 2994.

Lemelin, M., Lucey, P. G., Miljković, K., Gaddis, L. R., Hare, T., & Ohtake, M. (2019). The compositions of the lunar crust and upper mantle: Spectral analysis of the inner rings of lunar impact basins. *Planetary and Space Science*, *165*, 230–243. https://doi.org/10.1016/j.pss.2018.10.003.

Lemelin, M., Lucey, P. G., Neumann, G. A., Mazarico, E. M., Barker, M. K., Kakazu, A., et al. (2016). Improved calibration of reflectance data from the LRO Lunar Orbiter Laser Altimeter (LOLA) and implications for space weathering. *Icarus*, *273*, 315–328. https://doi.org/10.1016/j.icarus.2016.02.006.

Li, L., & Mustard, J. F. (2000). Compositional gradients across mare-highland contacts: Importance and geological implication of lateral transport. *Journal of Geophysical Research: Planets*, *105*(E8), 20431–20450. https://doi.org/10.1029/1999JE001168.

Li, L., & Mustard, J. F. (2003). Highland contamination in lunar mare soils: Improved mapping with multiple end-member spectral mixture analysis (MESMA). *Journal of Geophysical Research: Planets*, *108*(E6). https://doi.org/10.1029/2002JE001917.

Li, L., & Mustard, J. F. (2005). On lateral mixing efficiency of lunar regolith. *Journal of Geophysical Research: Planets*, *110*(E11). https://doi.org/10.1029/2004JE002295.

Lucey, P. G., Hinrichs, J., Kelly, M., Wellnitz, D., Izenberg, N., Murchie, S., et al. (2002). Detection of temperature-dependent spectral variation on the asteroid Eros and new evidence for the presence of an olivine-rich silicate assemblage. *Icarus*, *155*(1), 181–188. https://doi.org/10.1006/icar.2001.6747.

Lucey, P. G., Keil, K., & Whitely, R. (1998). The influence of temperature on the spectra of the A-asteroids and implications for their silicate chemistry. *Journal of Geophysical Research: Planets*, *103*(E3), 5865–5871. https://doi.org/10.1029/97JE03691.

Lucey, P. G., Neumann, G. A., Riner, M. A., Mazarico, E., Smith, D. E., Zuber, M. T., et al. (2014). The global albedo of the Moon at 1064 nm from LOLA. *Journal of Geophysical Research: Planets*, *119*(7), 2013JE004592. https://doi.org/10.1002/2013JE004592.

Lucey, P.G., Blewett, D.T., Taylor, G.J., & Hawke, B.R. (2000). Imaging of lunar surface maturity. *Journal of Geophysical Research: Planets*, *105*, 20377–20386. https://doi.org/10.1029/1999JE001110.

McEwen, A. S., & Robinson, M. S. (1995). Global albedo variations on the Moon: Clementine 750-nm observations. Abstracts of the Lunar and Planetary Science Conference, 26, 931.

Moroz, L., Schade, U., & Wäsch, R. (2000). Reflectance Spectra of Olivine–Orthopyroxene-Bearing Assemblages at Decreased Temperatures: Implications for Remote Sensing of Asteroids. *Icarus*, *147*(1), 79–93. https://doi.org/10.1006/icar.2000.6430.

Mustard, J. F., & Hays, J. E. (1997). Effects of hyperfine particles on reflectance spectra from 0.3 to 25 μm. *Icarus*, *125*(1), 145–163. https://doi.org/10.1006/icar.1996.5583.

Nelson, D. M., Koeber, S. D., Daud, K., Robinson, M. S., Watters, T. R., Banks, M. E., & Williams, N. R. (2014, March). Mapping lunar maria extents and lobate scarps using LROC image products. In Lunar and Planetary Science Conference (Vol. 45, p. 2861).

Neumann, G. A., Cavanaugh, J. F., Sun, X., Mazarico, E. M., Smith, D. E., Zuber, M. T., et al. (2013). Bright and dark polar deposits on Mercury: Evidence for surface volatiles. *Science*, *339*(6117), 296–300. https://doi.org/10.1126/science.1229764.

Noble, S.K., Pieters, C.M., Taylor, L.A., Morris, R.V., Allen, C.C., McKAY, D.S., & Keller, L.P. (2001). The optical properties of the finest fraction of lunar soil: Implications for space weathering. *Meteoritics & Planetary Science, 36*, 31–42. https://doi.org/10.1111/j.1945-5100.2001.tb01808.x.

Pieters, C. M. (1978). Mare basalt types on the front side of the Moon: A summary of spectral reflectance data. Lunar and Planetary Science Conference, 9th, Houston, Tex., 3, 2825–2849.

Pieters, C. M. (1983). Strength of mineral absorption features in the transmitted component of near-infrared reflected light: First results from RELAB. *Journal of Geophysical Research: Solid Earth*, *88*(B11), 9534–9544. https://doi.org/10.1029/JB088iB11p09534.

Pieters, C. M. (1986). Composition of the lunar highland crust from near-infrared spectroscopy. *Reviews of Geophysics*, *24*(3), 557–578. https://doi.org/10.1029/RG024i003p00557.

Pieters, C. M., & Noble, S. K. (2016). Space weathering on airless bodies. *Journal of Geophysical Research: Planets*, *121*(10), 2016JE005128. https://doi.org/10.1002/2016JE005128.

Pieters, C. M., Fischer, E. M., Rode, O., & Basu, A. (1993). Optical effects of space weathering: The role of the finest fraction. *Journal of Geophysical Research*, *98*(E11), 20817. https://doi.org/10.1029/93JE02467.

Pieters, C. M., Taylor, L. A., Noble, S. K., Keller, L. P., Hapke, B., Morris, R. V., et al. (2000). Space weathering on airless bodies: Resolving a mystery with lunar samples. *Meteoritics & Planetary Science*, *35*(5), 1101–1107. https://doi.org/10.1111/j.1945-5100.2000.tb01496.x.

Platz, T., Nathues, A., Schorghofer, N., Preusker, F., Mazarico, E., Schröder, S. E., et al. (2016). Surface water-ice deposits in the northern shadowed regions of Ceres. *Nature Astronomy*, *1*(1), 1–6. https://doi.org/10.1038/s41550-016-0007.

Roush, T. L., & Singer, R. B. (1986). Gaussian analysis of temperature effects on the reflectance spectra of mafic minerals in the 1-μm region. *Journal of Geophysical Research: Solid Earth*, *91*(B10), 10301–10308. https://doi.org/10.1029/JB091iB10p10301.

Roush, T. L., & Singer, R. B. (1987). Possible temperature variation effects on the interpretation of spatially resolved reflectance observations of asteroid surfaces. *Icarus*, *69*(3), 571–574. https://doi.org/10.1016/0019-1035(87)90026-1.

Schade, U., & Wäsch, R. (1999). NIR reflectance spectroscopy of mafic minerals in the temperature range between 80 and 473 K. *Advances in Space Research*, *23*(7), 1253–1256. https://doi.org/10.1016/S0273-1177(99)00193-3.

Singer, R. B., & Roush, T. L. (1985). Effects of temperature on remotely sensed mineral absorption features. *Journal of Geophysical Research: Solid Earth*, *90*(B14), 12434–12444. https://doi.org/10.1029/JB090iB14p12434.

Smith, D. E., Zuber, M. T., Frey, H. V., Garvin, J. B., Head, J. W., Muhleman, D. O., et al. (1998). Topography of the Northern Hemisphere of Mars from the Mars Orbiter Laser Altimeter. *Science*, *279*(5357), 1686–1692. https://doi.org/10.1126/science.279.5357.1686.

Smith, D. E., Zuber, M. T., Jackson, G. B., Cavanaugh, J. F., Neumann, G. A., Riris, H., et al. (2010). The Lunar Orbiter Laser Altimeter investigation on the Lunar Reconnaissance Orbiter mission. *Space Science Reviews*, *150*(1–4), 209–241. https://doi.org/10.1007/s11214-009-9512-y.

Smith, D. E., Zuber, M. T., Neumann, G. A., Mazarico, E., Lemoine, F. G., Head III, J. W., et al. (2017). Summary of the results from the Lunar Orbiter Laser Altimeter after seven years in lunar orbit. *Icarus*, *283*, 70–91. https://doi.org/10.1016/j.icarus.2016.06.006.

Varatharajan, I., Srivastava, N., & Murty, S.V.S. (2014). Mineralogy of young lunar mare basalts: Assessment of temporal and spatial heterogeneity using M3 data from Chandrayaan-1. *Icarus*, *236*, 56–71. https://doi.org/10.1016/j.icarus.2014.03.045.

Vasavada, A. R., Bandfield, J. L., Greenhagen, B. T., Hayne, P. O., Siegler, M. A., Williams, J.-P., & Paige, D. A. (2012). Lunar equatorial surface temperatures and regolith properties from the Diviner Lunar Radiometer Experiment. *Journal of Geophysical Research: Planets*, *117*(E12). https://doi.org/10.1029/2011JE003987.

Vasavada, A. R., Paige, D. A., & Wood, S. E. (1999). Near-surface temperatures on Mercury and the Moon and the stability of polar ice deposits. *Icarus*, *141*(2), 179–193. https://doi.org/10.1006/icar.1999.6175.

Williams, J.-P., Paige, D. A., Greenhagen, B. T., & Sefton-Nash, E. (2017). The global surface temperatures of the Moon as measured by the Diviner Lunar Radiometer Experiment. *Icarus*, *283*, 300–325. https://doi.org/10.1016/j.icarus.2016.08.012.

Yamashita, N., Gasnault, O., Forni, O., d'Uston, C., Reedy, R. C., Karouji, Y., et al. (2012). The global distribution of calcium on the Moon: Implications for high-Ca pyroxene in the eastern mare region. *Earth and Planetary Science Letters*, *353–354*, 93–98. https://doi.org/10.1016/j.epsl.2012.08.010.

Zuber, M. T., Head, J. W., Smith, D. E., Neumann, G. A., Mazarico, E., Torrence, M. H., et al. (2012). Constraints on the volatile distribution within Shackleton crater at the lunar south pole. *Nature*, *486*(7403), 378–381. https://doi.org/10.1038/nature11216.

Journal of Geophysical Research: Planets

Supporting Information for

Temperature-dependent changes in the normal albedo of the lunar surface at 1064 nm

Ariel N. Deutsch[1], Gregory A. Neumann[2], James W. Head[1], Paul G. Lucey[3]

[1]Department of Earth, Environmental and Planetary Sciences, Brown University, Providence RI 02912

[2]NASA Goddard Space Flight Center, Greenbelt, MD 20771

[3]Hawaii Institute of Geophysics and Planetology, University of Hawaii at Manoa, Honolulu, HI, 96822

Contents of this file

Introduction

The supplemental data provide additional information on the calibration of the reflectance data from the Lunar Orbiter Laser Altimeter (LOLA) instrument (Fig. S1) and details on the spread of LOLA data utilized in this statistical analysis (Table S1).

We analyze the normal albedo of the lunar surface using LOLA data acquired by Detector 3 on Laser 1 during the Nominal Mission Phase (LRO_NO_01 through LRO_NO_13) and the Science Mission Phase (LRO_SM_02 through LRO_SM_17). LOLA observations are corrected for drift in each LOLA mission month (Nominal Mission Phase (NO) or Science Mission Phase (SM)) by a cubic polynomial function with a step function offset between the NO and SM phases (Fig. S1). The linear fit to the regression intercept (in mission months) is polynomial:

$$Y_0 = -0.0407031024479 + 0.00150450253316 * \mathrm{m} \qquad \text{(Eq. S1)}.$$

For the nominal mission phases, the cubic fit to the regression slopes is:

$$Y_{phase} = 1.33324536294 + 0.00306123514405 * m - 0.0047453967058 * m^2 + 0.000101223404893 * m^3 \qquad \text{(Eq. S2)}.$$

For the science mission phases, the cubic fit to the regression slopes is:

$$Y_{phase} = 1.13324536294 + 0.00306123514405 * \mathrm{m} - 0.0047453967058 * \mathrm{m}^2 + 0.000101223404893 * \mathrm{m}^3 \quad \text{(Eq. S3)}.$$

The coefficients Y_0 and Y_{phase} are evaluated for each mission month subset and used to rescale the apparent reflectance to match the Lucey et al. (2016) map in the PDS via the formula:

$$[albedo] = \frac{[LOLA\_D3] - Y_0}{Y_{phase} - step} \quad \text{(Eq. S4)}.$$

where step=0 during Nominal Mission months and step = 0.2 during Science Mission months.

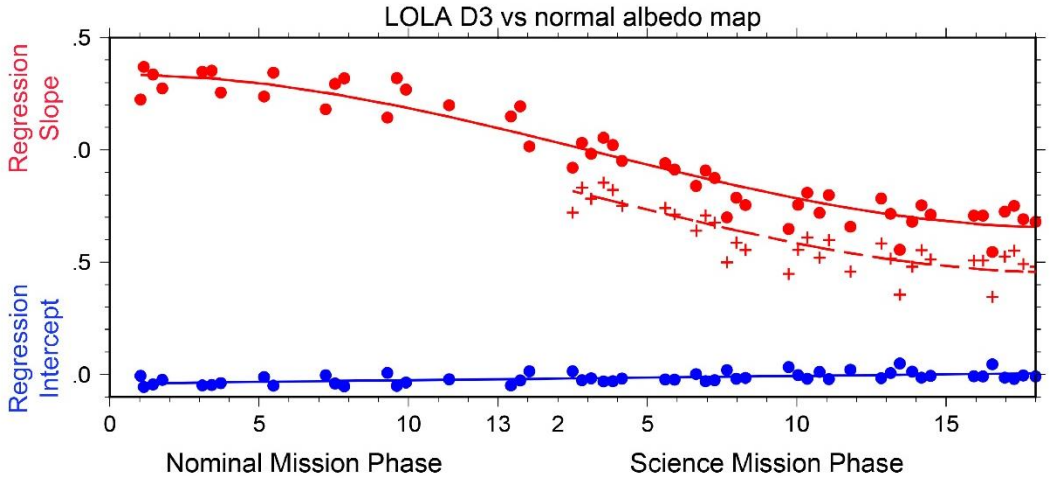

Figure S1. The blue symbols show the regression intercept and the red symbols show the regression slope. The regression coefficients are mapped to the fraction of the LOLA mission month that they represent. The plus symbols are the slope data before shifting upwards by a step-function to achieve a reasonable cubic fit.

Local Time	Mission Phase	Mission Month	Number of LOLA shots
08:00	NOMGRD	03	8858508
		09	12117607
	SCIGRD	03	10311044
		09	7809286
		10	3233635
		16	10967911
09:00	NOMGRD	09	8923350
	SCIGRD	02	9108857
		03	1999123
		09	11175819
		15	3099038
		16	6393027
10:00	NOMGRD	01	5055197

	SCIGRD	02	11197387
		09	1223020
		15	8141911
11:00	NOMGRD	01	5599733
		07	6174418
	SCIGRD	02	401127
		07	782747
		15	4925580
12:00	NOMGRD	01	68169
		07	11838993
		13	1239757
	SCIGRD	07	10682889
13:00	NOMGRD	01	691065
		07	4162239
		13	12625063
	SCIGRD	06	1617555
		07	8791281
		13	9019401
14:00	NOMGRD	13	8156525
	SCIGRD	06	11134889
		12	363418
		13	12392194
15:00	NOMGRD	05	8775505
	SCIGRD	05	4374966
		06	6293350
		12	8546987
		13	405022

Table S1. The number of individual LOLA observations utilized for this statistical analysis, divided by phase of data acquisition and local time of day.